Atomic multiplet and charge transfer screening effects in 1*s* and 2*p* core-level x-ray photoelectron spectra of early 3*d* transition-metal oxides

Tatsuya Yamaguchi,[1,*] Keisuke Higashi,[1,*] Anna Regoutz,[2] Yoshihiro Takahashi,[1] Masoud Lazemi,[3] Qijun Che,[3] Frank M. F. de Groot,[3] and Atsushi Hariki[1]

[1]*Department of Physics and Electronics, Graduate School of Engineering, Osaka Metropolitan University 1-1 Gakuen-cho, Nakaku, Sakai, Osaka 599-8531, Japan*

[2]*Department of Chemistry, University College London, 20 Gordon Street, London WC1H 0AJ, United Kingdom*

[3]*Materials Chemistry and Catalysis, Debye Institute for Nanomaterials Science, Utrecht University, Universiteitsweg 99, 3584 CG Utrecht, The Netherlands*

(Received 28 January 2024; revised 4 April 2024; accepted 3 May 2024; published 21 May 2024)

We present a comparative analysis of 1*s* and 2*p* core-level hard x-ray photoelectron spectroscopy (HAXPES) spectra of metallic VO_2 and CrO_2. Even though the V 1*s* and 2*p* spectra in VO_2 show similar line shapes except for the absence/presence of a spin-orbit splitting in the core levels, the Cr 1*s* and 2*p* spectra exhibit distinct main-line shapes. The experimental HAXPES spectra are analyzed by the Anderson impurity model based on the density functional theory + dynamical mean-field theory and a conventional MO_6 cluster model. We examine the interplay between the formation of the intra-atomic multiplet between a core hole and valence electrons and the charge-transfer effect on the chemical bonding followed by the 1*s* and 2*p* core electron excitations. We demonstrate the advantage of 1*s* HAXPES to the routinely employed 2*p* one for distinguishing contributions of a metal-ligand and metallic screening from a state near the Fermi level in metallic early 3*d* transition-metal oxides.

DOI: 10.1103/PhysRevB.109.205143

I. INTRODUCTION

Transition metal oxides (TMOs) exhibit a variety of functional properties ranging from unconventional superconductivity with high T_c to exotic phase transitions, including metal-insulator transitions [1,2]. These properties often arise from the complex interplay between local electron-electron interaction and interatomic hybridization. The formation of intra-atomic multiplet introduces additional complexity in multiorbital cases, resulting in nontrivial correlated states, even in metallic systems, such as Hund's metal [3–5]. Core-level x-ray photoelectron spectroscopy (XPS) is a powerful tool to investigate TMOs [6]. In XPS, a highly localized core hole created by x-ray irradiation strongly interacts with the *d* electrons on the same transition metal (TM) ion, leading to atomic multiplet fine structures in the XPS spectrum. Besides, the sudden appearance of the core hole induces a dynamical charge response from surrounding ions to the excited ion, traditionally called charge-transfer (CT) screening [7–9]. The CT screening often generates satellite peaks in the core-level spectra, providing valued insights into the chemical bonding properties. The development of hard x-ray photoelectron spectroscopy (HAXPES) has enabled the exploration of bulk properties and deeper core levels of materials compared to conventional soft x-rays [6,10–14].

Recently, TM 1*s* HAXPES spectra were examined for insulating late (NiO, Fe_2O_3) [9,15] and early 3*d* TMOs (TiO_2, $SrTiO_3$) [16–18]. For the band-insulating Ti oxides with a d^0 configuration in the formal valence, Ti 1*s* HAXPES revealed low-energy satellites that are not seen in the Ti $2p_{3/2}$ one, since the satellites are positioned at the same binding energies E_B as the Ti $2p_{1/2}$ spin-orbit-partner. In Fe_2O_3 (Mott insulator) and NiO (CT insulator), the 1*s* spectra clearly exhibit CT screening features, including a nonlocal CT channel from the distant Ni or Fe ions beyond the nearest-neighboring ligands [7,8,11,19], despite a larger lifetime broadening than the 2*p* core-level excitation [9,15]. These findings suggest the 1*s* core-level excitation as a complementary tool to the routinely used 2*p* excitation for studying 3*d* TMOs. However, the previous studies have exclusively focused on the insulators. In metallic TMOs, 2*p* HAXPES spectra often exhibit a metallic nonlocal screening feature (edge singularity) from a conducting state at the Fermi level, providing insights into the correlated metallic properties [11,20–28]. Yet, the metallic screening effect in 1*s* spectra has not been explored.

Another aspect in the 1*s* core-level excitation is the absence of the core-valence Coulomb multiplet effect, which would eliminate fine features and thus allow an easy access to the valence and chemical bonding information. However, this potential benefit of 1*s* HAXPES is not emphasized in the previous studies, primarily because the TM 3*d* shell is almost empty in $SrTiO_3$ and TiO_2, and largely occupied in NiO. In such cases, the core-valence multiplet effect is weak in the 2*p* XPS spectra. Thus, survey for other TM oxides with rich core-valence multiplet effect in the 2*p* spectra will be valuable to examine the benefit of the multiplet-free 1*s* excitation.

[*]These authors contributed equally to this work.

In this study, we present a systematic comparison of 1*s* and 2*p* HAXPES spectra of metallic vanadium dioxide (VO_2) and chromium dioxide (CrO_2). We examine the sensitivity of the 1*s* excitation to the metallic nonlocal screening and demonstrate difference in the 1*s* and 2*p* HAXPES spectra, where the core-valence atomic multiplet effect is not negligible in the 2*p* excitation.VO_2 exhibits a metallic behavior in the high-temperature rutile structure phase. The V 2*p* HAXPES spectrum displays a shoulder feature associated with the V $2p_{3/2}$ main line due to a metallic CT screening [23–25]. In the previous studies [23,24], the V 1*s* HAXPES spectrum exhibits a similar shoulder feature. CrO_2 is a half-metallic compound. Sperlich *et al.* [29] reported Cr 2*p* HAXPES of CrO_2, revealing a characteristic double-peak structure in the Cr $2p_{3/2}$ main line. The low-E_B feature in the double-peak structure is suppressed in a surface-sensitive soft x-ray spectrum, suggesting that a metallic CT screening is active in the 2*p* excitation. In this study, we conduct a HAXPES measurement of the Cr 1*s* core-level in CrO_2, and compare the 1*s* and 2*p* spectra. Though both oxides are textbook examples of correlated metals, recent advances in, e.g., heterostructure and thin-film engineering have promoted renewed interest in their electronic structure and core-level HAXPES spectra [30–33].

We simulate the experimental spectra using the Anderson impurity model (AIM) based on the local density approximation (LDA) + dynamical mean-field theory (DMFT) and conventional MO_6 cluster model. The LDA+DMFT method can be viewed as an extension of the MO_6 cluster model for computing the core-level XPS spectra. In this approach, the discrete ligand orbitals of the cluster model are replaced by a continuous metallic bath optimized within the LDA+DMFT scheme, which contains information about the entire lattice. Thus, the LDA+DMFT AIM represents the CT screening responses, including the nonlocal CT channels [9,19,34]. The cluster model considers only the CT screening from the nearest-neighboring oxygens, traditionally called local screening [6]. Thus, a comparison of the two models enables us to assess the contributions of the metallic nonlocal screening in the 1*s* and 2*p* spectra. The impurity model description allows us to consider the local core-valence multiplet interaction explicitly.

II. METHODS

The Cr 1*s* HAXPES of CrO_2 was measured at the HIKE station of the KMC-1 beamline at BESSY. A photon energy of 8.95 keV was used, and the energy resolution is ∼0.5 eV [9]. The CrO_2 sample was a commercially available crystalline CrO_2 powder (Magtrieve) [35]. The powder was ground using a mortar and pressed into a pill. The V 1*s* HAXPES spectrum of VO_2 was reproduced from the previous study [23].

The simulation of Cr (V) 1*s* and 2*p* HAXPES for CrO_2 (VO_2) starts with a standard LDA+DMFT calculation [36–38]. Both CrO_2 and VO_2 (metallic phase) crystallize in a rutile structure with space group $P4_2/mnm$ (No. 136). The experimental lattice parameters of $a = 4.421$ Å(4.556 Å) and $c = 2.916$ Å(2.859 Å) in CrO_2 (VO_2) [39,40] are adopted in this work. We perform an LDA calculation for the experimental crystal structure and subsequently construct a tight-binding model spanning both Cr (V) 3*d* and O 2*p* states from the LDA bands using Wien2K and wannier90 packages [41–43]. The tight-binding model is augmented with local electron-electron interaction within the TM 3*d* shell that is determined by Hubbard U and Hund's J parameters. We set these values to $(U, J) = (5.0\text{ eV}, 1.0\text{ eV})$ and (6.0 eV, 1.0 eV) for the Cr and V cases, respectively, consulting with previous density functional theory (DFT)-based and spectroscopy studies for chromium and vanadium oxides [44,45]. The strong-coupling continuous-time quantum Monte Carlo (CT-QMC) impurity solver [46–49] with density-density approximation to the on-site electron-electron interaction is used to obtain the self-energies $\Sigma(i\omega_n)$ of Cr (V) 3*d* electrons from the AIM. The double-counting correction $\mu_{\rm dc}$, which is introduced to subtract the *d*–*d* interaction effect present already in LDA step [37,50], is treated as an adjustable parameter and fixed to reproduce the experimental valence and core-level spectra. The $\mu_{\rm dc}$ dependence of the calculated spectra can be found in the Supplementary Material (SM) [51]. To compute valence spectra and hybridization densities $\Delta(\varepsilon)$ on the real-frequency axis, analytically continued $\Sigma(\varepsilon)$ in the real-frequency domain is obtained using the maximum entropy method [52]. We do not implement the charge self-consistency (updating the DFT charge) in the present LDA+DMFT calculation. Experimentally, VO_2 is a paramagnetic metal in a high-temperature phase [53] and CrO_2 is a ferromagnetic metal with a Curie temperature of approximately 390 K [54]. Thus, the calculations are performed for the paramagnetic phase for VO_2 and the ferromagnetic phase for CrO_2.

The Cr (V) 1*s* and 2*p* HAXPES spectra are computed from the AIM implementing the DMFT hybridization densities $\Delta(\varepsilon)$, following methods detailed in Refs. [9,19,55]. In this step, the AIM is extended to include the core orbitals and their interaction with the valence electrons. Though the core-valence interaction value U_{dc} is an adjustable parameter in this approach, an empirical relation $U_{dc} = 1.2 \sim 1.3 \times U_{dd}$ is well established for 3*d* TMOs, where U_{dd} represents the configuration-averaged interaction on the TM 3*d* shell [9,19]. In SM [51], we verified that varying U_{dc} within this range does not affect the spectra quantitatively, and thus it is set to $U_{dc} = 1.2 \times U_{dd}$ in the main result. The multipole term in the core-valence interaction is parameterized by the higher-order Slater integrals obtained from the atomic Hartree-Fock code. The atomic Slater integral values are reduced to 80% from the bare values to simulate the effect of intraatomic configuration interaction from higher basis configurations neglected in the atomic calculation. This treatment was successfully applied in modeling XPS as well as core-level x-ray absorption spectra in a wide range of 3*d* TM compounds [56–59]. For CrO_2, the simulations implementing different scaling factors (R_{2p-3d}) to the bare values are performed. The small spin-orbit coupling within the TM 3*d* shell ($\xi_{\rm soc} \sim 0.04$ eV) is ignored in the LDA+DMFT self-consistent calculations to avoid complex off-diagonal elements in $\Delta(\varepsilon)$ in the CT-QMC calculation for the AIM, while it is considered explicitly when computing the core-level HAXPES spectra. The spin-orbit coupling in the TM 2*p* shell is also considered, and the spin-orbit coupling constants are taken from the atomic calculation [9,19].

We employ the configuration-interaction (CI) solver for the AIM with the same implementation as described in Refs. [19,55,60]. In the MO_6 cluster-model calculation, the

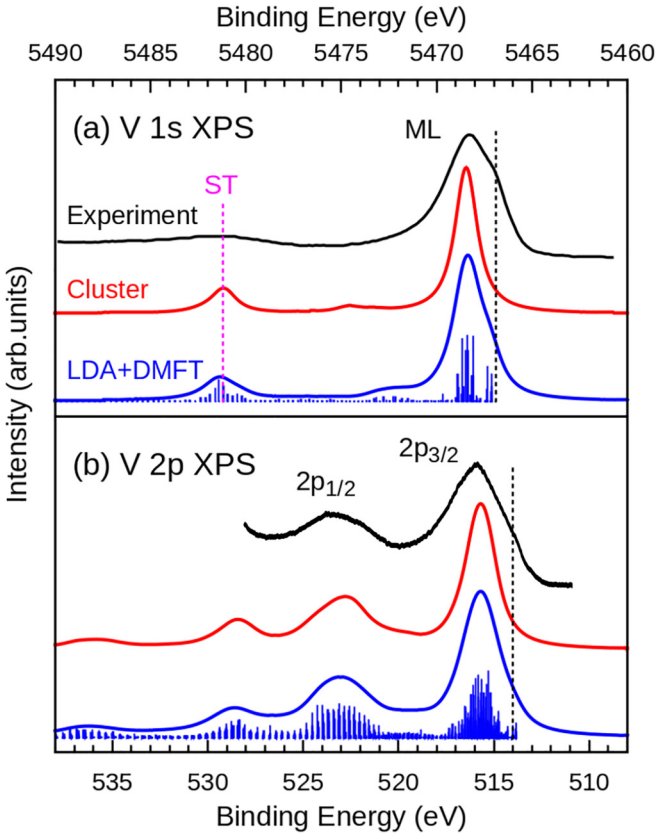

FIG. 1. The LDA+DMFT AIM (blue) and the VO_6 cluster model (red) calculations for (a) V 1*s* XPS and (b) V 2*p* XPS spectra for metallic VO_2 in the high-temperature rutile structure phase. The experimental HAXPES data are taken from Ref. [23]. The spectral intensities are convoluted with a Gaussian of 200 meV and a Lorentzian of 650 meV in the half width at half maximum (HWHM) for both 1*s* and 2*p* spectra. The main line (ML) and the satellite (ST) are indicated.

electron hopping amplitudes with the nearest-neighboring ligands are extracted from the tight-binding model constructed from the LDA bands mentioned above and summarized in Appendix B. The cluster model implements the same local Hamiltonian for the x-ray excited Cr (V) ion with the LDA+DMFT AIM. As noted in Refs. [18,55], care must be taken for the number of electronic configurations included to represent the XPS initial and final states within the CI scheme for a highly covalent system. We checked the convergence of the XPS spectral intensities as a function of the number of configurations in the studied compounds in Appendix B.

III. RESULTS

Figure 1 shows the V 1*s* and 2*p* XPS spectra of metallic VO_2 calculated by the LDA+DMFT AIM method and the VO_6 cluster model. The experimental 1*s* and 2*p* XPS data are reproduced from Ref. [23]. The LDA+DMFT valence-band spectra can be found in Appendix A. Apart from the presence of the V $2p_{1/2}$ spin-orbit component and a different lifetime broadening, the V 1*s* and $2p_{3/2}$ experimental spectra exhibit similar line shapes. A satellite (ST) feature is located approximately 13 eV above the main line (ML), as indicated by a dashed line.

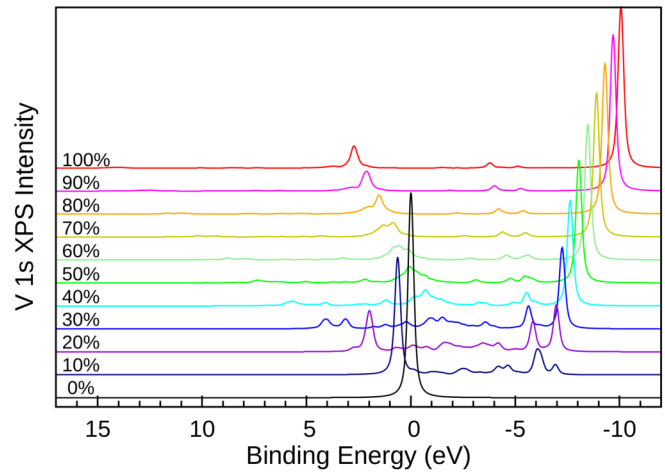

FIG. 2. V 1*s* XPS spectra simulated by the VO_6 cluster model with varying metal-ligand (V 3*d*–O 2*p*) hybridization strength. 100% corresponds to the hybridization strength derived from the LDA bands for the experimental rutile structure of VO_2 in Appendix B. The spectral intensities are convoluted with a Gaussian of 100 meV and a Lorentzian of 100 meV (HWHM).

The VO_6 cluster model represents the overall features in the V 1*s* and 2*p* spectra. In Fig. 2, the 1*s* spectra computed with varying the metal-ligand hybridization in the cluster model are shown. The diagonal energies of the electronic configurations in the final states are listed in Table I; see Appendix B for those in the initial state. Note that the screened $|\underline{c}d^2\underline{L}\rangle$ configuration has an energy lower than that of $|\underline{c}d^1\rangle$ due to the core-valence interaction U_{dc} for an excess *d* electron. The effective hybridization $V_{\rm eff}$ with the ligands can be given as $V_{\rm eff} = [(4 - N_{e_g}) \times V_{e_g}^2 + (6 - N_{t_{2g}}) \times V_{t_{2g}}^2]^{1/2}$, where N_{e_g} ($N_{t_{2g}}$) and V_{e_g} ($V_{t_{2g}}$) denote occupation of the e_g (t_{2g}) states and hybridization strength of the ligand and e_g (t_{2g}) orbitals [6,9,18,61]. For VO_2 (with $N_{t_{2g}} = 1$ and $N_{e_g} = 0$) in a formal valence state, $V_{\rm eff}$ accounts for 9.1 eV (Appendix B). The large hybridization leads to well-split bondinglike and antibondinglike states of the $|\underline{c}d^1\rangle$ and $|\underline{c}d^2\underline{L}\rangle$ states, forming the

TABLE I. The configuration (diagonal) energies in the V 1*s* XPS final states within the VO_6 cluster-model Hamiltonian in eV. Here, the charge-transfer energy is defined for a V^{4+} (d^1) electronic configuration as $\Delta_{\rm CT} = E(d^2\underline{L}) - E(d^1) = \varepsilon_d - \varepsilon_L + U_{dd}$, where ε_d (ε_L) denotes the averaged V 3*d* (ligand 2*p*) energy. The values of charge-transfer energy $\Delta_{\rm CT}$, $3d - 3d$ interaction U_{dd}, and $2p$-$3d$ core-valence interaction U_{dc} are found in Appendix B.

Conf.	Diagonal energies	Value
$\|\underline{c}d^1\rangle$	0	0.0
$\|\underline{c}d^2\underline{L}^1\rangle$	$\Delta_{\rm CT} - U_{dc}$	−4.7
$\|\underline{c}d^3\underline{L}^2\rangle$	$2\Delta_{\rm CT}+U_{dd} - 2U_{dc}$	−3.8
$\|\underline{c}d^4\underline{L}^3\rangle$	$3\Delta_{\rm CT}+3U_{dd} - 3U_{dc}$	2.7
$\|\underline{c}d^5\underline{L}^4\rangle$	$4\Delta_{\rm CT}+6U_{dd} - 4U_{dc}$	14.7
$\|\underline{c}d^6\underline{L}^5\rangle$	$5\Delta_{\rm CT}+10U_{dd} - 5U_{dc}$	32.3
$\|\underline{c}d^7\underline{L}^6\rangle$	$6\Delta_{\rm CT}+15U_{dd} - 6U_{dc}$	55.4

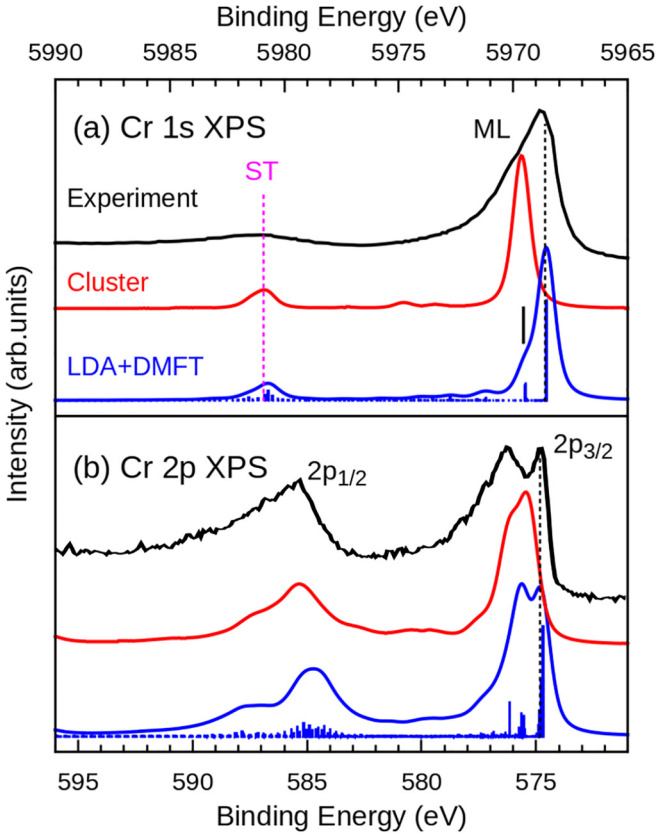

FIG. 3. The experimental HAXPES, the LDA+DMFT AIM (blue), and the CrO_6 cluster-model (red) calculations for (a) Cr 1*s* XPS and (b) Cr 2*p* XPS spectra. The spectral intensities are convoluted with a Gaussian and a Lorentzian of 300 and 250 meV (HWHM), respectively, for both 1*s* and 2*p* spectra. The experimental Cr 2*p* HAXPES data are taken from Ref. [29]. The main line (ML) and the satellite (ST) are indicated.

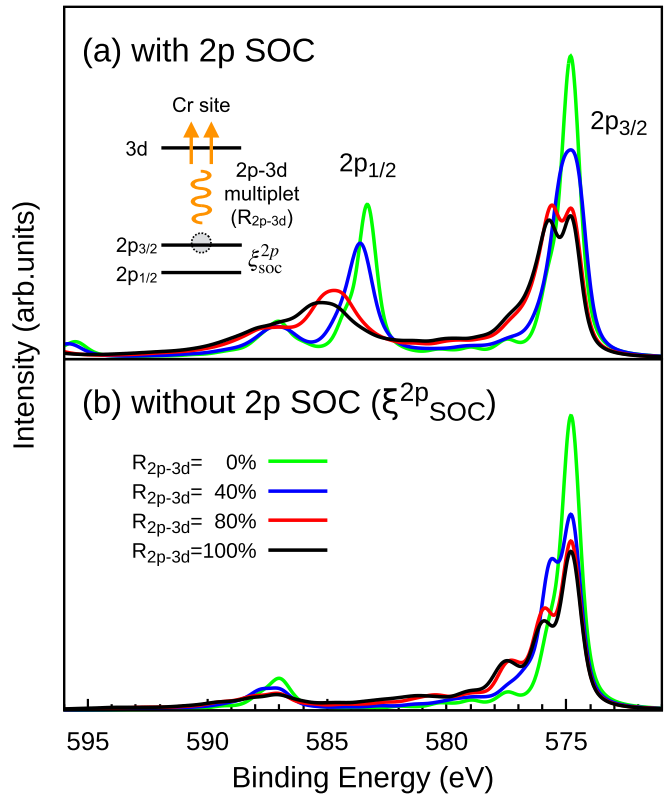

FIG. 4. (a) Cr 2*p* XPS spectral intensities calculated by the LDA+DMFT AIM method with reducing strength of the 2*p*–3*d* core-valence Coulomb multiplet interaction from the ionic values. (b) The calculated spectra without the spin-orbit coupling ($\xi^{2p}_{SOC} = 0$) on the 2*p* core orbitals. The spectral intensities are convoluted with a Gaussian and a Lorentzian of 300 and 250 meV (HWHM), respectively.

main line and satellite, respectively. Similar to Ti oxides [18], higher configurations up to $|\underline{c}d^5\underline{L}^4\rangle$ are necessary for accurate description of the satellites, as demonstrated in Appendix B.

Both the V 1*s* and $2p_{3/2}$ main lines exhibit a shoulder feature originating from metallic nonlocal CT screening at $E_B = 5467$ eV in 1*s* and $E_B = 514$ eV in $2p_{3/2}$, as indicated by the dotted lines in Fig. 1. The LDA+DMFT AIM reproduces the shoulder feature, while it is missing in the cluster-model result, as expected given that the former model includes a metallic CT screening, while the latter model considers only the metal-ligand one. Furthermore, the LDA+DMFT AIM yields a broad band feature around $E_B = 5472$ eV in the 1*s* spectrum, which shares similarities with the low-E_B satellites in Ti 1*s* HAXPES spectra of TiO_2 and $SrTiO_3$ [16–18]. Due to its overlap with the broad tail of the V $2p_{1/2}$, this feature is not clearly seen in the V $2p_{3/2}$ spectrum [Fig. 1(b)].

Next, we examine ferromagnetic metallic CrO_2. Figure 3 presents the Cr 1*s* and 2*p* XPS spectra calculated by the LDA+DMFT AIM and the CrO_6 cluster model. The Cr 2*p* experimental HAXPES spectrum is taken from Ref. [29]. The LDA+DMFT valence-band spectra can be found in Appendix A. The Cr $2p_{3/2}$ main line ($E_B \sim 576$ eV) exhibits the double-peak feature. Interestingly, the Cr 1*s* main line ($E_B \sim 5968.5$ eV) shows an asymmetric line shape, but not a double-peak feature as in the Cr $2p_{3/2}$ spectrum. This is a notable contrast with VO_2 (Fig. 1), as the V 1*s* and $2p_{3/2}$ spectra resemble each other. The LDA+DMFT results reproduce both the Cr 1*s* and 2*p* spectra reasonably well. The cluster model incorrectly yields a symmetric single-peak 1*s* main line and does not reproduce the double-peak feature in the Cr $2p_{3/2}$ main line (Fig. 3). This suggests the presence of metallic CT contributions in both the Cr 1s and 2*p* spectra of CrO_2 as in the VO_2 case. A detailed analysis of the spectra within the CrO_6 cluster model can be found in Appendix C.

To get insight into the different shapes in the 1*s* and 2*p* main line in CrO_2, we calculate the 2*p* spectra with modulating the multiplet coupling between the Cr 2*p* and 3*d* electrons in Fig. 4(a). Here, $R_{2p\text{-}3d}$ denotes a scaling factor for the multipole part in the Cr 2*p*-3*d* interaction in the LDA+DMFT AIM. The 2*p*-3*d* core-valence multiplet interaction significantly influences the $2p_{3/2}$ main-line shape. The 2*p* spectrum with $R_{2p\text{-}3d} = 0\%$ closely resembles the Cr 1*s* spectrum in Fig. 3(a). This indicates that the CT screening to the x-ray excited Cr from the rest of the crystal is essentially the same in the 1*s* and 2*p* excitations, which is not surprising, given that the hybridization strength of the Cr 3*d* states with the electron bath is determined in the valence electronic structure

when a core hole is absent. However, the $2p$-$3d$ multiplet interaction at the x-ray excited Cr site mixes the screened states via different CT channels substantially, and consequently the intrinsic CT spectral peaks are distributed in a complex way in the $2p$ spectrum in the case of CrO_2. The $1s$ excitation, with negligibly weak core-valence interaction, is thus better suited for examining and quantifying the CT effect.

In the $1s$ spectrum, the prominent peak at the low-E_B side (∼5968.5 eV, dashed line) dominantly consists of the metallic-screening states, while the high-E_B feature (∼5969.5 eV, solid bar) contains mostly the local-screening states from ligands. Only the latter CT channel can be captured in the CrO_6 cluster model [see Fig. 3(a)]. The LDA+DMFT AIM result indicates that the intrinsic spectral intensity of the metallic screening is substantial compared to the local screening one upon the core-level excitation, manifesting in the observed asymmetric line shape in the experimental $1s$ data. However, the intensities of the two CT features are largely modulated due to the strong $2p$-$3d$ multiplet interaction in the $2p$ spectrum. Thus, the double peaks in the $2p_{3/2}$ spectrum do not serve as a good measure of the two CT channels.

Figure 4(b) shows the $2p$ XPS spectra calculated with eliminating the spin-orbit interaction on the Cr $2p$ shell in the LDA+DMFT AIM Hamiltonian. The spin-orbit interaction plays a marginal role for the $2p_{3/2}$ main-line shape and does not affect the spectra in the absence of the $2p$-$3d$ interaction ($R_{2p\text{-}3d} = 0\%$). Thus, the $2p$-$3d$ core-valence multiplet interaction is the decisive factor for the difference in the Cr $1s$ and $2p$ spectra.

IV. CONCLUDING REMARKS

In this study, we have analyzed $1s$ and $2p$ core-level HAXPES spectra of metallic VO_2 and CrO_2, archetypal correlated metallic $3d$ transition-metal oxides. We conducted a HAXPES measurement for the $1s$ core level of CrO_2. While the V $1s$ spectrum in VO_2 closely resembles the $2p_{3/2}$ spectrum in the literature, we find the Cr $1s$ main line in CrO_2, exhibiting asymmetric line shape, substantially differs from the Cr $2p_{3/2}$ main line with the double peaks. Through a comprehensive computational analysis for the $1s$ and $2p$ spectra of VO_2 and CrO_2 using the LDA+DMFT AIM method and conventional MO_6 cluster model, we demonstrated that the difference in the CrO_2 and VO_2 spectra originates from a strong core-valence atomic multiplet effect in the $2p$ excitation of CrO_2. The double peaks in the Cr $2p_{3/2}$ main line do not directly represent either of the metallic-screening or metal-ligand CT final states, as these CT final states are mixed by the multiplet interaction acting locally at the x-ray excited Cr site. The core-valence multiplet-free $1s$ spectrum unveils intrinsic spectral features of the metallic and metal-ligand CT screenings upon the core-level excitation. Our LDA+DMFT AIM calculation for the $1s$ spectra reveals that the spectral intensity of the metallic screening dominates that of the metal-ligand screening, highlighting the advantage of $1s$ excitation in characterizing correlated metallic $3d$ TMOs, especially when the atomic multiplet effect is not negligible in the $2p$ spectra. Future systematic investigations of the $1s$ HAXPES spectra for $3d$ TMOs with the active $2p$-$3d$ multiplets, such as Co or Mn oxides, would be of interest.

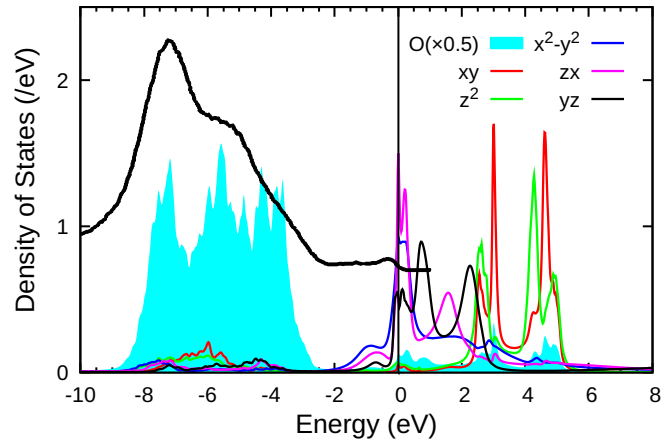

FIG. 5. The LDA+DMFT valence spectral intensities for metallic bulk VO_2. The experimental valence-band XPS spectrum measured at 320 K is taken from Ref. [23].

ACKNOWLEDGMENTS

A.H. thanks H. Fujiwara for fruitful discussions. A.H. was supported by JSPS KAKENHI under Grants No. 21K13884, No. 21H01003, No. 23K03324, No. 23H03816, and No. 23H03817.

APPENDIX A: LDA+DMFT VALENCE SPECTRA

Figure 5 shows valence-band spectra of metallic VO_2 calculated by the LDA+DMFT method, together with the experimental valence-band XPS spectrum taken from Ref. [23]. As previously discussed in Ref. [62], while the single-site DMFT lacks the V-V intersite self-energy needed for describing the dimerized insulating phase with a monoclinic structure, it provides a reasonable description for the correlated metallic phase of the high-temperature rutile-structure phase. Our DMFT valence-band spectrum is similar to the cluster DMFT

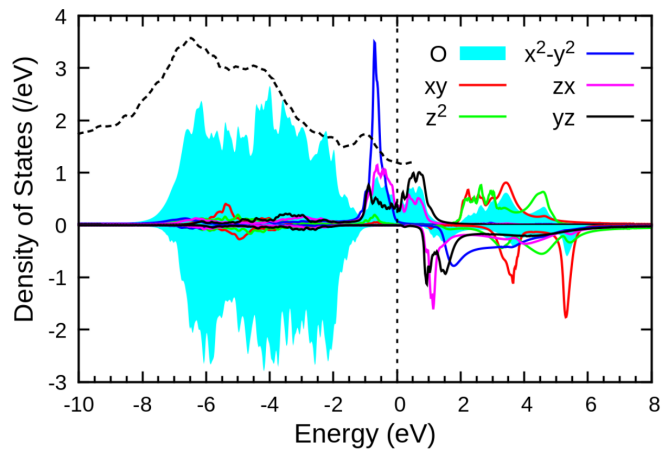

FIG. 6. The LDA+DMFT valence spectral intensities for bulk CrO_2. The experimental valence-band XPS spectrum (dashed) measured at 150 K is taken from Ref. [29].

TABLE II. The parameter values for (configuration-averaged) $3d$-$3d$ (U_{dd}) and $2p$-$3d$ (U_{dc}) interactions and the metal-ligand hybridization amplitude adopted in the VO_6 and CrO_6 cluster models in eV unit.

	U_{dd}	U_{dc}	$V_{B_{1g}}$	V_{A_g}	$V_{A'_g}$	$V_{B_{2g}}$	$V_{B_{3g}}$
VO_2	5.56	6.67	3.80	3.83	2.08	2.10	2.23
CrO_2	4.56	5.47	3.58	3.72	1.93	1.70	1.90

result for the metallic phase [45,62]. The LDA+DMFT spectrum exhibits a lower Hubbard-band feature around -1 eV and a quasiparticle feature near the Fermi energy E_F. The calculated binding energies E_B of the O $2p$ states with respect to the V $3d$ states match well with the experimental data, supporting the used value of the double-counting correction $\mu_{\rm dc}$ in the LDA+DMFT calculation. In Fig. 6, the LDA+DMFT valence-band spectra of CrO_2 together with the experimental valence-band XPS spectrum taken from Ref. [29] is also shown. The double-counting dependence of the valence spectra of VO_2 and CrO_2 can be found in the SM [51].

APPENDIX B: MODEL PARAMETERS IN THE CLUSTER-MODEL CALCULATION

Table II summarizes the parameter values employed in our cluster-model calculations for VO_2 and CrO_2. The interaction parameters U_{dd} and U_{dc} are set to the same values as the ones in the LDA+DMFT AIM Hamiltonian for VO_2 and CrO_2. The one-particle parameters, i.e., electron hopping amplitudes and crystal-field energies, are derived from the tight-binding models constructed from the DFT bands for the experimental structures.

The hopping amplitudes between the V (Cr) d orbitals [$B_{1g}(xy)$, $A_g(3z^2-r^2)$, $A'_g(x^2-y^2)$, $B_{2g}(zx)$ and $B_{3g}(yz)$] and the molecular orbitals consisting of the nearest-neighboring ligand $2p$ orbitals with the same symmetry are given in Table II. The charge-transfer energy $\Delta_{\rm CT}$ is taken from Refs. [63,64]. Table III summarizes the diagonal energies of the electronic configurations considered in the VO_6 and CrO_6 cluster model accounting for the interaction U_{dd} and the charge-transfer energy $\Delta_{\rm CT}$ up to the $|d^7\underline{L}^6\rangle$ configuration. Figure 7 shows the V and Cr $1s$ XPS spectra calculated by the cluster model with increasing the number of the electronic configurations included in representing the initial and final states. Table IV summarizes the weights of the electronic configurations. The position of the satellites is converged well with the basis set including up to the $|d^5\underline{L}^4\rangle$ configuration for VO_2 and the $|d^6\underline{L}^4\rangle$ configuration for CrO_2. We also checked the convergence of the LDA+DMFT AIM spectra with respect to the number of the electronic configurations included in the configuration-interaction solver evaluation [19,55] of the spectral intensities.

TABLE III. Configuration (diagonal) energies in the initial states of VO_6 (left) and CrO_6 (right) cluster models in eV unit.

Conf.	VO_2	Val.	Conf.	CrO_2	Value
$\|d^1\rangle$	0	0.0	$\|d^2\rangle$	0	0.0
$\|d^2\underline{L}^1\rangle$	$\Delta_{\rm CT}$	2.0	$\|d^3\underline{L}^1\rangle$	$\Delta_{\rm CT}$	1.0
$\|d^3\underline{L}^2\rangle$	$2\Delta_{\rm CT}+U_{dd}$	9.6	$\|d^4\underline{L}^2\rangle$	$2\Delta_{\rm CT}+U_{dd}$	6.6
$\|d^4\underline{L}^3\rangle$	$3\Delta_{\rm CT}+3U_{dd}$	22.7	$\|d^5\underline{L}^3\rangle$	$3\Delta_{\rm CT}+3U_{dd}$	16.7
$\|d^5\underline{L}^4\rangle$	$4\Delta_{\rm CT}+6U_{dd}$	41.4	$\|d^6\underline{L}^4\rangle$	$4\Delta_{\rm CT}+6U_{dd}$	31.4
$\|d^6\underline{L}^5\rangle$	$5\Delta_{\rm CT}+10U_{dd}$	65.6	$\|d^7\underline{L}^5\rangle$	$5\Delta_{\rm CT}+10U_{dd}$	50.6
$\|d^7\underline{L}^6\rangle$	$6\Delta_{\rm CT}+15U_{dd}$	95.4	$\|d^8\underline{L}^6\rangle$	$6\Delta_{\rm CT}+15U_{dd}$	74.4

TABLE IV. Weights of the configurations in the ground-state wave function of VO_2 (upper) and CrO_2 (bottom) in the VO_6 and CrO_6 cluster-model simulations for different basis sets (3, 4, 5, 6, and 7 configurations in the basis expansions).

VO_2	3conf.	4conf.	5conf.	6conf.	7conf.
$\|d^1\rangle$	0.317	0.248	0.243	0.237	0.237
$\|d^2\underline{L}^1\rangle$	0.522	0.487	0.485	0.477	0.477
$\|d^3\underline{L}^2\rangle$	0.161	0.232	0.232	0.240	0.240
$\|d^4\underline{L}^3\rangle$	–	0.033	0.038	0.043	0.043
$\|d^5\underline{L}^4\rangle$	–	–	0.002	0.003	0.003
$\|d^6\underline{L}^5\rangle$	–	–	–	0.000	0.000
$\|d^7\underline{L}^6\rangle$	–	–	–	–	0.000
CrO_2	3conf.	4conf.	5conf.	6conf.	7conf.
$\|d^2\rangle$	0.308	0.226	0.212	0.211	0.211
$\|d^3\underline{L}^1\rangle$	0.508	0.460	0.446	0.445	0.445
$\|d^4\underline{L}^2\rangle$	0.184	0.270	0.279	0.280	0.280
$\|d^5\underline{L}^3\rangle$	–	0.044	0.058	0.059	0.059
$\|d^6\underline{L}^4\rangle$	–	–	0.004	0.005	0.005
$\|d^7\underline{L}^5\rangle$	–	–	–	0.000	0.000
$\|d^8\underline{L}^6\rangle$	–	–	–	–	0.000

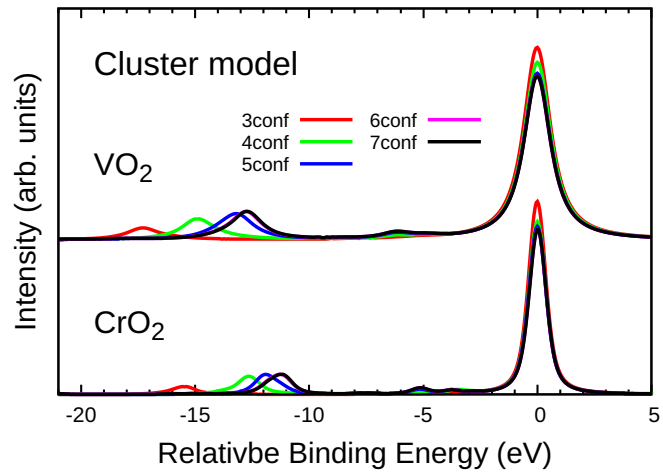

FIG. 7. The V (Cr) $1s$ XPS spectra calculated by the VO_6 (CrO_6) cluster model with varying the number of electronic configurations included in the spectral calculation. Here, the spectral intensities are convoluted with a Gaussian of 200 (300) meV and a Lorenzian of 650 (250) meV for VO_2 (CrO_2) (HWHM).

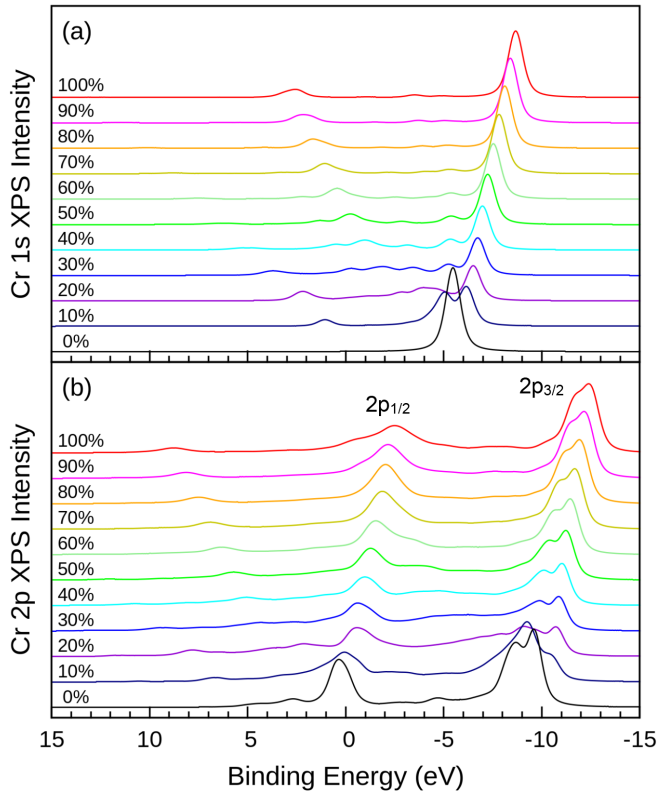

FIG. 8. (a) Cr 1*s* and (b) 2*p* XPS spectra simulated by the CrO_6 cluster model with varying the metal-ligand (Cr 3*d*-O 2*p*) hybridization strength. 100% corresponds to the hybridization strength derived from the LDA bands for the experimental crystal structure (see Appendix B). The spectral intensities are convoluted with a Gaussian of 300 meV and a Lorenzian of 250 meV (HWHM).

TABLE V. The configuration (diagonal) energies in the Cr 1*s* XPS final states within the CrO_6 cluster-model Hamiltonian in eV. Here, the charge-transfer energy is defined for a Cr^{4+} (d^2) electronic configuration as $\Delta_{CT} = E(d^3\underline{L}) - E(d^2) = \varepsilon_d - \varepsilon_L + 2U_{dd}$, where ε_d (ε_L) denotes the averaged Cr 3*d* (ligand 2*p*) energy. The values of charge-transfer energy Δ_{CT}, 3*d*-3*d* interaction U_{dd}, and 2*p*-3*d* core-valence interaction U_{dc} are found in Appendix B.

Conf.	Diagonal energies	Value
$\|\underline{c}d^2\rangle$	0	0.0
$\|\underline{c}d^3\underline{L}^1\rangle$	$\Delta_{CT} - U_{dc}$	−4.5
$\|\underline{c}d^4\underline{L}^2\rangle$	$2\Delta_{CT} + U_{dd} - 2U_{dc}$	−4.4
$\|\underline{c}d^5\underline{L}^3\rangle$	$3\Delta_{CT} + 3U_{dd} - 3U_{dc}$	0.3
$\|\underline{c}d^6\underline{L}^4\rangle$	$4\Delta_{CT} + 6U_{dd} - 4U_{dc}$	9.5
$\|\underline{c}d^7\underline{L}^5\rangle$	$5\Delta_{CT} + 10U_{dd} - 5U_{dc}$	23.3
$\|\underline{c}d^8\underline{L}^6\rangle$	$6\Delta_{CT} + 15U_{dd} - 6U_{dc}$	41.6

APPENDIX C: CrO_6 CLUSTER-MODEL SIMULATION OF THE Cr 2*p* XPS SPECTRA

In Fig. 8, we calculate the Cr 1*s* and 2*p* XPS spectra with changing the Cr-O orbital hybridization strength in the CrO_6 cluster model. The configuration energies in the XPS final states within the cluster-model Hamiltonian are summarized in Table V. In the atomic limit (0%), i.e., $V = 0$, the Cr 2*p* XPS shows richer multiplet peaks in both the $2p_{3/2}$ and $2p_{1/2}$ components due to the strong Cr 2*p*-3*d* multipole interaction. The Cr-O hybridization renormalizes substantially the multiplet peaks [Fig. 3(b)]. The negligibly weak multiplet effect on the 1*s* excitation yields a quasi-single-peak line in the atomic limit [Fig. 3(a)].

[1] M. Imada, A. Fujimori, and Y. Tokura, Metal-insulator transitions, Rev. Mod. Phys. **70**, 1039 (1998).

[2] D. I. Khomskii, *Transition Metal Compounds* (Cambridge University, Cambridge, England, 2014).

[3] L. de' Medici, J. Mravlje, and A. Georges, Janus-faced influence of Hund's rule coupling in strongly correlated materials, Phys. Rev. Lett. **107**, 256401 (2011).

[4] K. M. Stadler, Z. P. Yin, J. von Delft, G. Kotliar, and A. Weichselbaum, Dynamical mean-field theory plus numerical renormalization-group study of spin-Orbital separation in a three-band Hund metal, Phys. Rev. Lett. **115**, 136401 (2015).

[5] A. Georges, L. d. Medici, and J. Mravlje, Strong correlations from Hund's coupling, Annu. Rev. Condens. Matter Phys. **4**, 137 (2013).

[6] F. de Groot and A. Kotani, *Core Level Spectroscopy of Solids* (CRC, Boca Raton, FL, 2008).

[7] M. van Veenendaal, Competition between screening channels in core-level x-ray photoemission as a probe of changes in the ground-state properties of transition-metal compounds, Phys. Rev. B **74**, 085118 (2006).

[8] M. A. van Veenendaal and G. A. Sawatzky, Nonlocal screening effects in 2*p* x-ray photoemission spectroscopy core-level line shapes of transition metal compounds, Phys. Rev. Lett. **70**, 2459 (1993).

[9] M. Ghiasi, A. Hariki, M. Winder, J. Kuneš, A. Regoutz, T.-L. Lee, Y. Hu, J.-P. Rueff, and F. M. F. de Groot, Charge-transfer effect in hard x-ray 1*s* and 2*p* photoemission spectra: LDA + DMFT and cluster-model analysis, Phys. Rev. B **100**, 075146 (2019).

[10] M. Taguchi, Y. Takata, and A. Chainani, Hard x-ray photoelectron spectroscopy: A few recent applications, J. Electron Spectrosc. Relat. Phenom. **190**, 242 (2013).

[11] M. Taguchi and G. Panaccione, Depth-dependence of electron screening, charge carriers and correlation: Theory and experiments, in *Hard X-ray Photoelectron Spectroscopy (HAXPES)*, edited by J. C. Woicik (Springer, Cham, 2016), pp. 197–216.

[12] F. Borgatti, P. Torelli, and G. Panaccione, Hard X-ray photoelectron spectroscopy of transition metal oxides: Bulk compounds and device-ready metal-oxide interfaces, J. Electron Spectrosc. Relat. Phenom. **208**, 95 (2016).

[13] C. Kalha, N. K. Fernando, P. Bhatt, F. O. L. Johansson, A. Lindblad, H. Rensmo, L. Z. Medina, R. Lindblad, S. Siol, L. P. H. Jeurgens, C. Cancellieri, K. Rossnagel, K. Medjanik, G. Schönhense, M. Simon, A. X. Gray, S. Nemšák, P. Lömker, C. Schlueter, and A. Regoutz, Hard x-ray photoelectron spectroscopy: A snapshot of the state-of-the-art in 2020, J. Phys.: Condens. Matter **33**, 233001 (2021).

[14] K. Kobayashi, Hard x-ray photoemission spectroscopy, Nucl. Instrum. Methods Phys. Res., Sect. A **601**, 32 (2009).

[15] J. Rubio-Zuazo, A. Chainani, M. Taguchi, D. Malterre, A. Serrano, and G. R. Castro, Electronic structure of FeO, $\gamma - Fe_2O_3$, and Fe_3O_4 epitaxial films using high-energy spectroscopies, Phys. Rev. B **97**, 235148 (2018).

[16] J. C. Woicik, C. Weiland, C. Jaye, D. A. Fischer, A. K. Rumaiz, E. L. Shirley, J. J. Kas, and J. J. Rehr, Charge-transfer satellites and chemical bonding in photoemission and x-ray absorption of $SrTiO_3$ and rutile TiO_2: Experiment and first-principles theory with general application to spectroscopic analysis, Phys. Rev. B **101**, 245119 (2020).

[17] J. C. Woicik, C. Weiland, and A. K. Rumaiz, Loss for photoemission versus gain for auger: Direct experimental evidence of crystal-field splitting and charge transfer in photoelectron spectroscopy, Phys. Rev. B **91**, 201412(R) (2015).

[18] A. Hariki, K. Higashi, T. Yamaguchi, J. Li, C. Kalha, M. Mascheck, S. K. Eriksson, T. Wiell, F. M. F. de Groot, and A. Regoutz, Satellites in the Ti 1*s* core level spectra of $SrTiO_3$ and TiO_2, Phys. Rev. B **106**, 205138 (2022).

[19] A. Hariki, T. Uozumi, and J. Kuneš, LDA + DMFT approach to core-level spectroscopy: Application to 3*d* transition metal compounds, Phys. Rev. B **96**, 045111 (2017).

[20] K. Horiba, M. Taguchi, A. Chainani, Y. Takata, E. Ikenaga, D. Miwa, Y. Nishino, K. Tamasaku, M. Awaji, A. Takeuchi, M. Yabashi, H. Namatame, M. Taniguchi, H. Kumigashira, M. Oshima, M. Lippmaa, M. Kawasaki, H. Koinuma, K. Kobayashi, T. Ishikawa *et al.*, Nature of the well screened state in hard x-ray Mn 2*p* core-level photoemission measurements of $La_{1-x}Sr_xMnO_3$ films, Phys. Rev. Lett. **93**, 236401 (2004).

[21] M. Taguchi, A. Chainani, M. Matsunami, R. Eguchi, Y. Takata, M. Yabashi, K. Tamasaku, Y. Nishino, T. Ishikawa, S. Tsuda, S. Watanabe, C.-T. Chen, Y. Senba, H. Ohashi, K. Fujiwara, Y. Nakamura, H. Takagi, and S. Shin, Anomalous state sandwiched between Fermi liquid and charge ordered Mott-insulating phases of Ti_4O_7, Phys. Rev. Lett. **104**, 106401 (2010).

[22] M. Taguchi, A. Chainani, N. Kamakura, K. Horiba, Y. Takata, M. Yabashi, K. Tamasaku, Y. Nishino, D. Miwa, T. Ishikawa, S. Shin, E. Ikenaga, T. Yokoya, K. Kobayashi, T. Mochiku, K. Hirata, and K. Motoya, Bulk screening in core-level photoemission from Mott-Hubbard and charge-transfer systems, Phys. Rev. B **71**, 155102 (2005).

[23] R. Eguchi, M. Taguchi, M. Matsunami, K. Horiba, K. Yamamoto, Y. Ishida, A. Chainani, Y. Takata, M. Yabashi, D. Miwa, Y. Nishino, K. Tamasaku, T. Ishikawa, Y. Senba, H. Ohashi, Y. Muraoka, Z. Hiroi, and S. Shin, Photoemission evidence for a Mott-Hubbard metal-insulator transition in VO_2, Phys. Rev. B **78**, 075115 (2008).

[24] S. Suga, A. Sekiyama, S. Imada, T. Miyamachi, H. Fujiwara, A. Yamasaki, K. Yoshimura, K. Okada, M. Yabashi, K. Tamasaku, A. Higashiya, and T. Ishikawa, ∼8 keV photoemission of the metal–insulator transition system VO_2, New J. Phys. **11**, 103015 (2009).

[25] G. J. Paez, C. N. Singh, M. J. Wahila, K. E. Tirpak, N. F. Quackenbush, S. Sallis, H. Paik, Y. Liang, D. G. Schlom, T.-L. Lee, C. Schlueter, W.-C. Lee, and L. F. J. Piper, Simultaneous structural and electronic transitions in epitaxial $VO_2/TiO_2(001)$, Phys. Rev. Lett. **124**, 196402 (2020).

[26] M. Taguchi, A. Chainani, K. Horiba, Y. Takata, M. Yabashi, K. Tamasaku, Y. Nishino, D. Miwa, T. Ishikawa, T. Takeuchi, K. Yamamoto, M. Matsunami, S. Shin, T. Yokoya, E. Ikenaga, K. Kobayashi, T. Mochiku, K. Hirata, J. Hori, K. Ishii *et al.*, Evidence for suppressed screening on the surface of high temperature $La_{2-x}Sr_xCuO_4$ and $Nd_{2-x}Ce_xCuO_4$ superconductors, Phys. Rev. Lett. **95**, 177002 (2005).

[27] M. W. Haverkort, G. Sangiovanni, P. Hansmann, A. Toschi, Y. Lu, and S. Macke, Bands, resonances, edge singularities and excitons in core level spectroscopy investigated within the dynamical mean-field theory, Europhys. Lett. **108**, 57004 (2014).

[28] P. S. Cornaglia and A. Georges, Theory of core-level photoemission and the x-ray edge singularity across the Mott transition, Phys. Rev. B **75**, 115112 (2007).

[29] M. Sperlich, C. König, G. Güntherodt, A. Sekiyama, G. Funabashi, M. Tsunekawa, S. Imada, A. Shigemoto, K. Okada, A. Higashiya, M. Yabashi, K. Tamasaku, T. Ishikawa, V. Renken, T. Allmers, M. Donath, and S. Suga, Intrinsic correlated electronic structure of CrO_2 revealed by hard x-ray photoemission spectroscopy, Phys. Rev. B **87**, 235138 (2013).

[30] D. Mondal, S. R. Mahapatra, A. M. Derrico, R. K. Rai, J. R. Paudel, C. Schlueter, A. Gloskovskii, R. Banerjee, A. Hariki, F. M. F. DeGroot, D. D. Sarma, A. Narayan, P. Nukala, A. X. Gray, and N. P. B. Aetukuri, Modulation-doping a correlated electron insulator, Nat. Commun. **14**, 6210 (2023).

[31] N. B. Aetukuri, A. X. Gray, M. Drouard, M. Cossale, L. Gao, A. H. Reid, R. Kukreja, H. Ohldag, C. A. Jenkins, E. Arenholz, K. P. Roche, H. A. Dürr, M. G. Samant, and S. S. P. Parkin, Control of the metal–insulator transition in vanadium dioxide by modifying orbital occupancy, Nat. Phys. **9**, 661 (2013).

[32] D. Shiga, X. Cheng, T. T. Kim, T. Kanda, N. Hasegawa, M. Kitamura, K. Yoshimatsu, and H. Kumigashira, Electronic phase diagram of Cr-doped VO_2 epitaxial films studied by *in situ* photoemission spectroscopy, Phys. Rev. B **108**, 045112 (2023).

[33] H. Fujiwara, K. Terashima, M. Sunagawa, Y. Yano, T. Nagayama, T. Fukura, F. Yoshii, Y. Matsuura, M. Ogata, T. Wakita, K. Yaji, A. Harasawa, K. Kuroda, S. Shin, K. Horiba, H. Kumigashira, Y. Muraoka, and T. Yokoya, Origins of thermal spin depolarization in half-metallic ferromagnet CrO_2, Phys. Rev. Lett. **121**, 257201 (2018).

[34] K. Higashi, T. Yamaguchi, Y. Takahashi, and A. Hariki, Charge-transfer effect in Fe 2*p* core-level x-ray photoemission spectra of trivalent Fe oxides: LDA + DMFT study, J. Phys.: Condens. Matter **34**, 375602 (2022).

[35] Sigma-Aldrich, Magtrieve supplementary information (2015), https://www.sigmaaldrich.com/JP/ja/product/aldrich/480037.

[36] A. Georges, G. Kotliar, W. Krauth, and M. J. Rozenberg, Dynamical mean-field theory of strongly correlated fermion systems and the limit of infinite dimensions, Rev. Mod. Phys. **68**, 13 (1996).

[37] G. Kotliar, S. Y. Savrasov, K. Haule, V. S. Oudovenko, O. Parcollet, and C. A. Marianetti, Electronic structure calculations with dynamical mean-field theory, Rev. Mod. Phys. **78**, 865 (2006).

[38] J. Kuneš, I. Leonov, M. Kollar, K. Byczuk, V. I. Anisimov, and D. Vollhardt, Dynamical mean-field approach to materials with strong electronic correlations, Eur. Phys. J.: Spec. Top. **180**, 5 (2009).

[39] M. S. Anwar and J. Aarts, Anomalous transport in half-metallic ferromagnetic CrO_2, Phys. Rev. B **88**, 085123 (2013).

[40] D. B. McWhan, M. Marezio, J. P. Remeika, and P. D. Dernier, X-ray diffraction study of metallic VO_2, Phys. Rev. B **10**, 490 (1974).

[41] P. Blaha, K. Schwarz, G. Madsen, D. Kvasnicka, and J. Luitz, *WIEN2k, An Augmented Plane Wave+Local Orbitals Program for Calculating Crystal Properties* (Karlheinz Schwarz, Technische Universität Wien, Austria, 2018).

[42] J. Kuneš, R. Arita, P. Wissgott, A. Toschi, H. Ikeda, and K. Held, Wien2wannier: From linearized augmented plane waves to maximally localized Wannier functions, Comput. Phys. Commun. **181**, 1888 (2010).

[43] A. A. Mostofi, J. R. Yates, G. Pizzi, Y.-S. Lee, I. Souza, D. Vanderbilt, and N. Marzari, An updated version of wannier90: A tool for obtaining maximally-localised Wannier functions, Comput. Phys. Commun. **185**, 2309 (2014).

[44] L. Craco, M. S. Laad, and E. Müller-Hartmann, Orbital Kondo effect in CrO_2: A combined local-spin-density-approximation dynamical-mean-field-theory study, Phys. Rev. Lett. **90**, 237203 (2003).

[45] W. H. Brito, M. C. O. Aguiar, K. Haule, and G. Kotliar, Metal-insulator transition in VO_2: A DFT + DMFT perspective, Phys. Rev. Lett. **117**, 056402 (2016).

[46] P. Werner, A. Comanac, L. de' Medici, M. Troyer, and A. J. Millis, Continuous-time solver for quantum impurity models, Phys. Rev. Lett. **97**, 076405 (2006).

[47] L. Boehnke, H. Hafermann, M. Ferrero, F. Lechermann, and O. Parcollet, Orthogonal polynomial representation of imaginary-time Green's functions, Phys. Rev. B **84**, 075145 (2011).

[48] H. Hafermann, K. R. Patton, and P. Werner, Improved estimators for the self-energy and vertex function in hybridization-expansion continuous-time quantum Monte Carlo simulations, Phys. Rev. B **85**, 205106 (2012).

[49] A. Hariki, A. Yamanaka, and T. Uozumi, Theory of spin-state selective nonlocal screening in Co $2p$ x-ray photoemission spectrum of $LaCoO_3$, J. Phys. Soc. Jpn. **84**, 073706 (2015).

[50] M. Karolak, G. Ulm, T. Wehling, V. Mazurenko, A. Poteryaev, and A. Lichtenstein, Double counting in LDA + DMFT—The example of NiO, J. Electron Spectrosc. Relat. Phenom. **181**, 11 (2010).

[51] See Supplemental Material at http://link.aps.org/supplemental/10.1103/PhysRevB.109.205143 for double-counting dependence of the LDA+DMFT valence-band spectra.

[52] M. Jarrell and J. Gubernatis, Bayesian inference and the analytic continuation of imaginary-time quantum Monte Carlo data, Phys. Rep. **269**, 133 (1996).

[53] F. J. Morin, Oxides which show a metal-to-insulator transition at the Neel temperature, Phys. Rev. Lett. **3**, 34 (1959).

[54] T. J. Swoboda, J. Arthur, Paul, N. L. Cox, J. N. Ingraham, A. L. Oppegard, and M. S. Sadler, Synthesis and properties of ferromagnetic chromium oxide, J. Appl. Phys. **32**, S374 (1961).

[55] M. Winder, A. Hariki, and J. Kuneš, X-ray spectroscopy of the rare-earth nickelate $LuNiO_3$: LDA + DMFT study, Phys. Rev. B **102**, 085155 (2020).

[56] F. M. F. de Groot, J. C. Fuggle, B. T. Thole, and G. A. Sawatzky, $2p$ x-ray absorption of $3d$ transition-metal compounds: An atomic multiplet description including the crystal field, Phys. Rev. B **42**, 5459 (1990).

[57] M. Matsubara, T. Uozumi, A. Kotani, and J. C. Parlebas, Charge transfer excitation in resonant x-ray emission spectroscopy of NiO, J. Phys. Soc. Jpn. **74**, 2052 (2005).

[58] J. Sugar, Potential-barrier effects in photoabsorption. II. Interpretation of photoabsorption resonances in lanthanide metals at the $4d$-electron threshold, Phys. Rev. B **5**, 1785 (1972).

[59] A. Tanaka and T. Jo, Temperature dependence of $2p$-core x-ray absorption spectra in $3d$ transition-metal compounds, J. Phys. Soc. Jpn. **61**, 2040 (1992).

[60] A. Hariki, M. Winder, T. Uozumi, and J. Kuneš, LDA + DMFT approach to resonant inelastic x-ray scattering in correlated materials, Phys. Rev. B **101**, 115130 (2020).

[61] T. Uozumi, K. Okada, A. Kotani, R. Zimmermann, P. Steiner, S. Hüfner, Y. Tezuka, and S. Shin, Theoretical and experimental studies on the electronic structure of M_2O_3 (M = Ti, V, Cr, Mn, Fe) compounds by systematic analysis of high-energy spectroscopy, J. Electron Spectrosc. Relat. Phenom. **83**, 9 (1997).

[62] S. Biermann, A. Poteryaev, A. I. Lichtenstein, and A. Georges, Dynamical singlets and correlation-assisted Peierls transition in VO_2, Phys. Rev. Lett. **94**, 026404 (2005).

[63] T. Uozumi, K. Okada, and A. Kotani, Electronic structures of Ti and V oxides: Calculation of valence photoemission and bremsstrahlung isochromat spectra, J. Phys. Soc. Jpn. **62**, 2595 (1993).

[64] C. F. Chang, D. J. Huang, A. Tanaka, G. Y. Guo, S. C. Chung, S.-T. Kao, S. G. Shyu, and C. T. Chen, Electronic structure of CrO_2 studied by magnetic circular dichroism in resonant photoemission, Phys. Rev. B **71**, 052407 (2005).